Nucleic Acids Research, 2025, **53**, gkae1314
https://doi.org/10.1093/nar/gkae1314
Advance access publication date: 20 January 2025
RNA and RNA-protein complexes

Cryo-EM structure of human TUT1:U6 snRNA complex

Seisuke Yamashita * **and Kozo Tomita** *

Department of Computational Biology and Medical Sciences, Graduate School of Frontier Sciences, The University of Tokyo, 5-1-5, Kashiwanoha, Kashiwa, Chiba 277-8562, Japan

*To whom correspondence should be addressed. Email: yamashita-s@edu.k.u-tokyo.ac.jp
Correspondence may also be addressed to Kozo Tomita. Tel: +81 471363611; Email: kozo-tomita@edu.k.u-tokyo.ac.jp

Abstract

U6 snRNA (small nuclear ribonucleic acid) is a ribozyme that catalyzes pre-messenger RNA (pre-mRNA) splicing and undergoes epitranscriptomic modifications. After transcription, the 3′-end of U6 snRNA is oligo-uridylylated by the multi-domain terminal uridylyltransferase (TUTase), TUT1. The 3′- oligo-uridylylated tail of U6 snRNA is crucial for U4/U6 di-snRNP (small nuclear ribonucleoprotein) formation and pre-mRNA splicing. Here, we present the cryo-electron microscopy structure of the human TUT1:U6 snRNA complex. The AUA-rich motif between the 5′-short stem-loop and the telestem of U6 snRNA is clamped by the N-terminal zinc finger (ZF)–RNA recognition motif and the catalytic Palm of TUT1, and the telestem is gripped by the N-terminal ZF and the Fingers, positioning the 3′-end of the telestem in the catalytic pocket. The internal stem-loop in the 3′-stem-loop of U6 snRNA is anchored by the C-terminal kinase-associated 1 domain, preventing U6 snRNA from dislodging on the TUT1 surface during oligo-uridylylation. TUT1 recognizes the sequence and structural features of U6 snRNA, and holds the entire U6 snRNA body using multiple domains to ensure oligo-uridylylation. This highlights the specificity of TUT1 as a U6 snRNA-targeting TUTase.

Graphical abstract

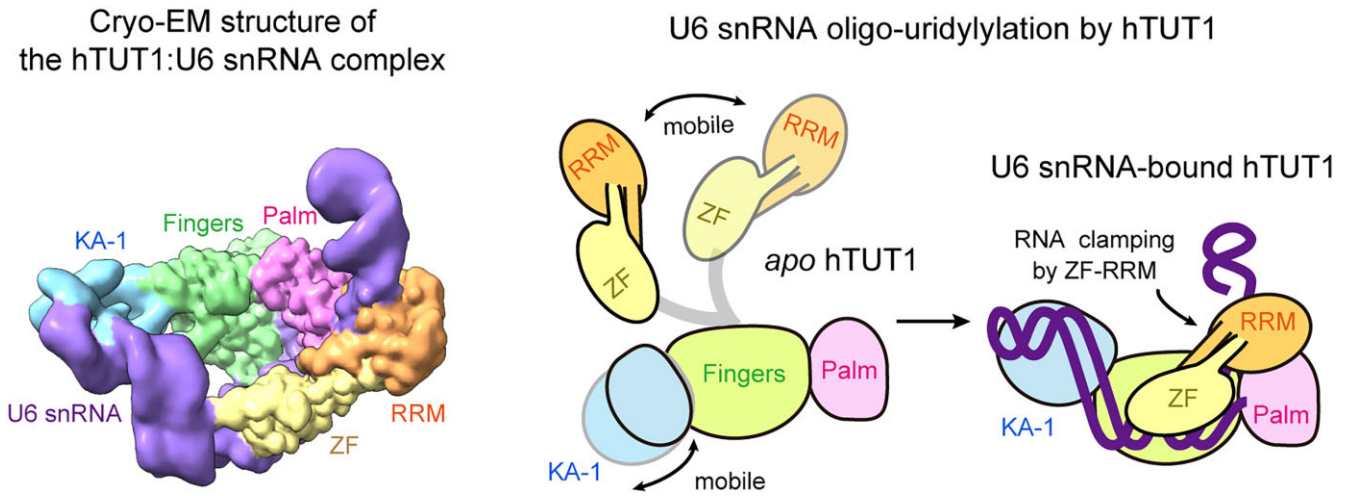

Introduction

Eukaryotic pre-messenger RNA (pre-mRNA) splicing is catalyzed by the spliceosome, a large ribonucleoprotein complex. The major spliceosome includes five small ribonucleoprotein (snRNP) complexes (the U1, U2, U4, U5 and U6 snRNPs) and numerous proteins (1). The U6 snRNP consists of U6 snRNA (small nuclear ribonucleic acid), p110 (hPrp24) and the LSm2–8 ring protein complex. p110 and LSm2–8 catalyze the annealing of U6 snRNA to U4 snRNA to form the U4/U6 di-snRNP (2–4). Subsequently, the U4/U6 di-snRNP is transformed into the U4/U6/U5 tri-snRNP, which is then recruited into the pre-spliceosome composed of the pre-mRNA and the U1 and U2 snRNPs. The U6 snRNA pairs with the U2 snRNA, and participates in the active site formation and catalysis of the splicing reactions (5).

The U6 snRNA is a catalytic RNA responsible for pre-mRNA splicing (5) and undergoes various post-transcriptional processes, including chemical modification of nucleosides and the addition of nucleotides at its termini (6,7), during its maturation process. After transcription by RNA polymerase III, the 3′-end of U6 snRNA is oligo-uridylylated by the terminal uridylyltransferase (TUTase),

Received: September 5, 2024. **Revised:** December 14, 2024. **Editorial Decision:** December 20, 2024. **Accepted:** December 26, 2024

TUT1 (TENT1), a member of the TENT family of proteins (8–13). Subsequently, the oligo-uridylylated tail is trimmed by MpnI (UsbI), a 3′–5′ exonuclease, to five uridines with a 2′, 3′-cyclic phosphate (UUUUU > p) (14–16). The oligo-uridylylated tail of U6 snRNA serves as the binding site for the LSm2–8 ring protein complex (17,18), facilitating the annealing of the U6 and U4 snRNAs to form the di-U4/U6 snRNA complex and contributing to efficient pre-mRNA splicing.

Human TUT1 (hTUT1) is a multi-domain protein consisting of an N-terminal zinc finger (ZF), an RNA recognition motif (RRM), central catalytic Palm and Fingers and a C-terminal kinase-associated 1 (KA-1) domain (19,20) (Figure 1A). Human U6 snRNA consists of two stem-loop secondary structures: a 5′-short stem-loop and a 3′-long stem-loop, flanked by a short single-stranded AUA motif (Figure 1B). The 3′-long stem-loop is composed of the telestem and the internal stem-loop (ISL), which are flanked by a mispaired/bulged region (21,22).

Our previous crystallographic and biochemical studies of truncated hTUT1 proteins, lacking the C-terminal KA-1 domain (hTUT1_ΔC) or the N-terminal ZF domain and RRM (hTUT1_ΔN), and hTUT1_ΔC in complex with a short U6 snRNA lacking the ISL and 5′-stem-loop (U6_mini) (20,23), suggested that specific sequences and structural features of U6 snRNA are recognized by the multi-domain hTUT1. However, the structure of full-length hTUT1 in complex with full-length U6 snRNA has not been reported, and the mechanisms of the recognition and oligo-uridylylation of full-length U6 snRNA by the multi-domain hTUT1 have remained enigmatic.

In this study, we present the cryo-electron microscopy (cryo-EM) structure of full-length hTUT1 in complex with full-length U6 snRNA. The structure provides a comprehensive picture, detailing how the structured U6 snRNA is specifically recognized and oligo-uridylylated by the multi-domain TUT1, and highlighting hTUT1 as a U6 snRNA-specific TUTase.

Materials and methods

Plasmid construction

The synthetic DNA encoding the hTUT1 gene was purchased from Eurofins Genomics (Japan). The nucleotide sequence of the synthetic hTUT1 gene is provided in Supplementary Table S1. The DNA fragment encoding full-length hTUT1 was cloned between the NdeI and XhoI sites of the pET22b vector (Merck Millipore, Japan). The amino acid sequence of recombinant hTUT1 is shown in Supplementary Table S1. The nucleotide sequences of the synthetic U6 snRNA gene and its variants used for *in vitro* transcription and the nucleotide sequences of the RNAs transcribed are listed in Supplementary Table S2. The nucleotide sequences of primers used in this study are listed in Supplementary Table S3.

Expression and purification of recombinant hTUT1 protein

Escherichia coli BL21(DE3) (Novagen, Japan) was transformed with the plasmid expressing hTUT1 (or its variant) and cultured in LB medium containing 50 μg/ml ampicillin at 37°C until the absorbance at 600 nm (A_{600}) reached 1.0. Expression of the hTUT1 protein (or its variant) was induced by adding 0.1 mM isopropyl-β-D-thiogalactopyranoside, and the culture was continued at 18°C for 16 h. The harvested cells were lysed in buffer, containing 20 mM Tris–HCl pH 7.0, 500 mM NaCl, 10 mM β-mercaptoethanol, 20 mM imidazole, 0.1 mM phenylmethylsulfonyl fluoride and 5% (v/v) glycerol. The proteins were first purified using a Ni-NTA agarose column (QIAGEN, Japan), followed by purification on a Hi-Trap Heparin HP column (GE Healthcare, Japan). Finally, the proteins were separated on a Hi-Load 16/60 Superdex 200 column (GE Healthcare, Japan), in buffer containing 20 mM Tris–HCl pH 7.0, 300 mM NaCl and 10 mM β-mercaptoethanol. The purified proteins were concentrated and stored at −80°C.

RNA synthesis and preparation

Synthetic human U6 snRNA and its variants were synthesized by T7 RNA polymerase, using the corresponding DNA fragments as templates *in vitro* (24). To obtain U6 snRNA (or its variants) with a homogeneous 3′-end, the DNA sequence corresponding to the HDV (hepatitis delta virus) ribozyme was placed downstream of the U6 snRNA gene (or its variants) (25) (Supplementary Table S2). The reaction mixture, containing 40 mM Tris–HCl pH 8.0, 14 mM $MgCl_2$, 2 mM ATP, 2 mM GTP, 2 mM CTP, 2 mM UTP, 10 mM GMP, 1 mM spermidine, 5 mM DTT, 0.01% (v/v) Triton X-100, 100 μg/ml template DNA and 10 μg/ml T7 RNA polymerase, was incubated at 37°C for 5 h. After *in vitro* transcription, the RNA was extracted with phenol-chloroform and dissolved in buffer, containing 10 mM Tris–HCl pH 7.0 and 20 mM $MgCl_2$. The RNA solution was subjected to 15 cycles of incubation (60°C for 3 min followed by 25°C for 3 min) to allow the 3′-end HDV ribozyme to self-cleave and release the U6 snRNA (or its variants) with a homogeneous 3′-end. The 2′,3′-cyclic phosphate group of the U6 snRNA (or its variants) was removed by T4 polynucleotide kinase (Takara, Japan), in buffer containing 50 mM MES pH 5.8, 20 mM $MgCl_2$ and 10 mM DTT. Finally, the U6 snRNA (or its variants) with a homogeneous 3′-end was purified by 10% (w/v) polyacrylamide gel electrophoresis under denaturing conditions. After gel purification, the structural homogeneity of the RNAs was confirmed by 10% (w/v) polyacrylamide gel electrophoresis under non-denaturing conditions, where the RNAs appeared as a single band. These purified RNAs were then used for the experiments. The synthetic nucleotide sequences of the U6 snRNA gene and its variants used for *in vitro* transcription, and the nucleotide sequences of U6 snRNA and its variants are listed in Supplementary Table S2.

Cryo-EM grid preparation and data collection

The hTUT1:U6 snRNA complex was reconstituted by mixing equimolar amounts of hTUT1 and U6 snRNA (12.5 μM each). The complex was separated using a Superdex 200 Increase 10/300 column (GE Healthcare, Japan), in buffer containing 20 mM Tris–HCl pH 7.0, 200 mM NaCl, 2 mM $MgCl_2$ and 10 mM β-mercaptoethanol. Fractions containing both hTUT1 and U6 snRNA were concentrated and stored at −80°C. Before grid preparation, the hTUT1:U6 snRNA concentration was adjusted to 0.5 mg/ml and the sample was supplemented with 0.005% (v/v) Tween 20 (final concentration).

The cryo-EM grids were glow-discharged using a PIB-10 (Vacuum Device, Japan) for 30 s at 8 mA. An aliquot (3 μl) of the hTUT1:U6 snRNA complex was applied to the grids at

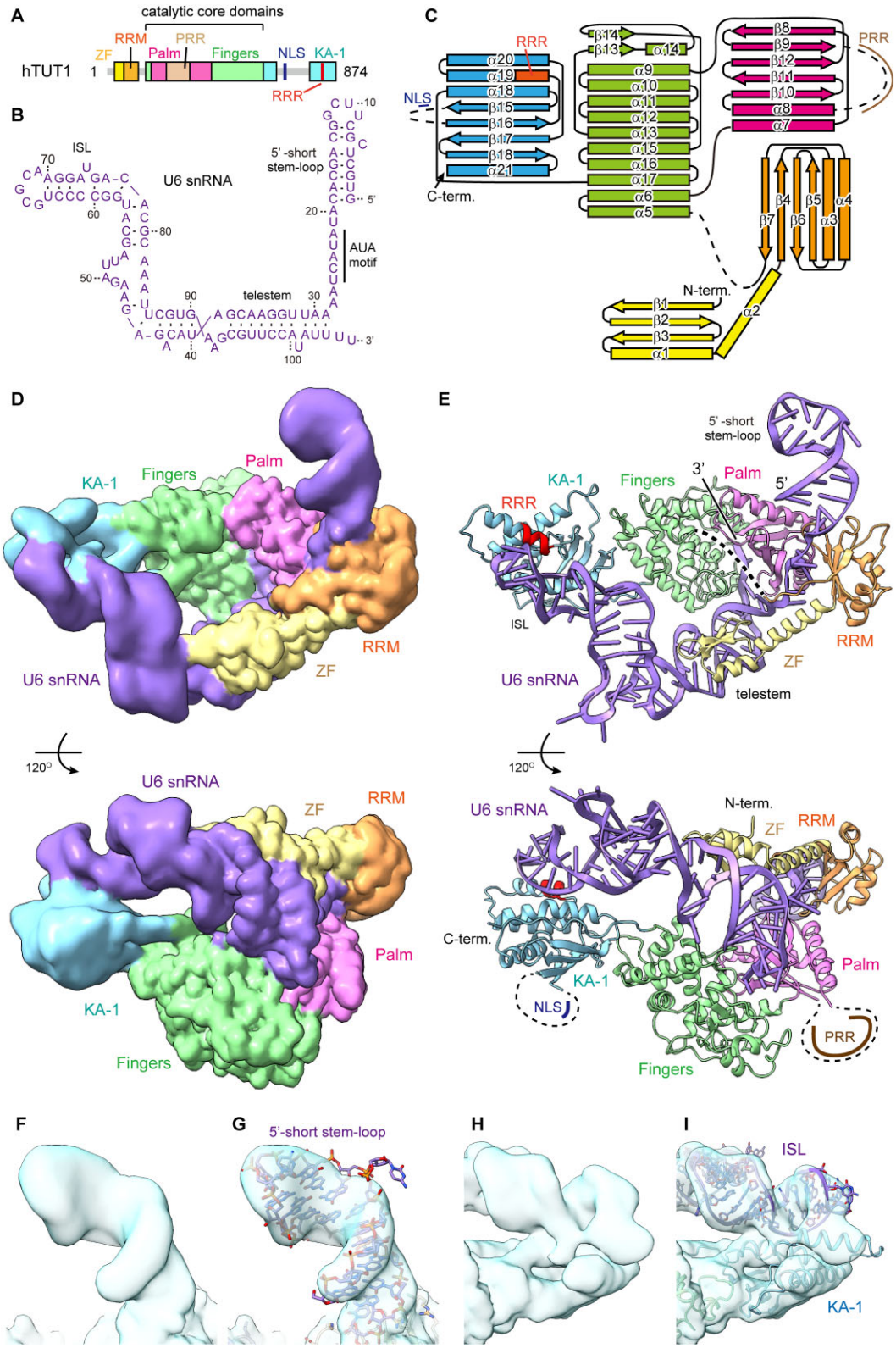

Figure 1. Overall structure of the hTUT1:U6 snRNA complex. (**A**) Schematic diagram of full-length hTUT1. ZF, RRM, Palm, Fingers and KA-1 are colored yellow, orange, magenta, green and cyan, respectively. (**B**) Schematic diagram of full-length U6 snRNA (106 nt). (**C**) Schematic view of the secondary structure of hTUT1. Each domain is colored as in panel (A). (**D**) Composite map of the hTUT1:U6 snRNA complex. (**E**) Cartoon representation of the overall structure of the hTUT1:U6 snRNA complex. ZF, RRM, Palm, Fingers and KA-1 of hTUT1 are colored as in panel (A), and U6 snRNA is colored purple. The flexible linkers in the Palm and KA-1 domains are not model-built, and shown as dotted lines (NLS:nuclear localization signal and PRR: proline-rich region). (**F**) Composite maps of the 5′-short stem-loop. (**G**) The model fitting into the maps in panel (F). (**H**) Composite maps of the KA-1 domain and the ISL of U6 snRNA. (**I**) The model fitting into the map in panel (H).

4°C under 100% humidity with a blot force of 10 for 4 s, and then plunge-frozen in liquid ethane using a Mark IV Vitrobot (Thermo Fisher Scientific).

Cryo-EM data were collected using Titan Krios G3i or G4 microscopes (Thermo Fisher Scientific), operated at 300 kV and equipped with a GIF Quantum-LS Energy Filter and a K3 Summit direct electron detector (Gatan, Inc.). Two datasets were collected and merged: one obtained using a Quantifoil Cu R1.3/1.2 #300 (Quantifoil) grid and Titan Krios G3i (Thermo Fisher Scientific), and the other using an UltrAuFoil #300 (Quantifoil) grid and a Titan Krios G4 (Thermo Fisher Scientific). Datasets were collected with a pixel size of 0.83 Å (nominal magnification: ×105 000) under a total exposure of 50 electrons/Å^2. The defocus range was set between −0.8 and −1.8 μm. A total of 5903 and 9967 movies were acquired for the Quantifoil Cu and UltrAuFoil grids, respectively.

Image processing

The data were processed using CryoSPARC (version 4.4.1) (26). Movie stacks were motion-corrected (27) and contrast-transfer functions were estimated. Particles were picked and selected through several rounds of 2D classification. Following *ab initio* reconstruction and non-uniform refinement, reference-based motion correction was applied to polish the particles. Further particle selection was performed using 2D classification and heterogeneous refinement, yielding a high-resolution consensus map at 3.21 Å resolution. While the core region of the hTUT1:U6 snRNA complex showed a well-resolved cryo-EM map, the regions corresponding to the 5′-short stem-loop and ISL of U6 snRNA, as well as the KA-1 domain of hTUT1, exhibited relatively weak cryo-EM maps. To improve the corresponding maps, 3D classification was performed with two focused masks: one for the 5′-short stem-loop of U6 snRNA (mask-1) and another for the ISL of U6 snRNA and the KA-1 domain of hTUT1 (mask-2). The 3D classifications were performed with the following parameters: target resolution: 6 Å, force hard classification: true, number of classes: 6, initialization mode: input and convergence criterion (%): 1%. The resultant maps provided detailed structural features for the corresponding regions for mask-1 and mask-2. The resolutions for the hTUT1:U6 snRNA structures encompassing the core and the mask-1 or mask-2 region were 3.83 and 3.72 Å, respectively. The three maps were post-processed with EMReady (28) and combined to create a composite map, which was used for model building and figure preparation. The workflow for the data processing and the evaluation of the cryo-EM maps is shown in Supplementary Figures S1 and S2, respectively, and representative cryo-EM maps are shown in Supplementary Figure S3.

Model building and refinement

For building the hTUT1:U6 snRNA complex model, the structures of truncated forms of hTUT1 (hTUT1_ΔN or hTUT1_ΔC) (PDB IDs: 5WU1, 5WU6) and hTUT1_ΔN in complex with short U6 snRNA (U6_mini) (PDB ID: 8IDF) (23) were manually docked into the cryo-EM map. The remaining part of the U6 snRNA model was initially constructed using RNAcomposer (29) and then manually model-built with Coot (30). Structure refinements were performed using Phenix (31,32). The statistics for the cryo-EM analysis and refinement are summarized in Table 1. Figures were prepared using UCSF ChimeraX (version 1.5) (33).

Uridylylation assays

A 60-μl reaction mixture, containing 50 mM Tris–HCl pH 8.5, 100 mM NaCl, 10 mM $MgCl_2$, 10 mM β-mercaptoethanol, 1 mM UTP and the specified concentrations of U6 snRNA (and its variants) transcript and hTUT1 (or its variants), was incubated at 37°C. At the indicated time points, 10-μl aliquots of the reaction mixture were withdrawn and the reaction was stopped. The RNAs were separated by 10% (w/v) polyacrylamide gel electrophoresis under denaturing conditions and stained with ethidium bromide. Bands were visualized and their intensities were quantified using a Gel Doc EZ system with the Image Lab software (Bio-Rad, Japan).

Gel-shift assay

RNAs (20 nM U6_snRNA and its variants) were mixed with varying concentrations (0–200 nM) of hTUT1_FL or hTUT1_ΔC in a 10-μl reaction buffer containing 50 mM Tris–HCl pH 8.5, 100 mM NaCl, 10 mM $MgCl_2$, 10 mM β-mercaptoethanol and 10% (v/v) glycerol. The mixture was incubated at room temperature for 15 min. The RNAs were then separated by 7.5% (w/v) polyacrylamide gel electrophoresis under native conditions at room temperature, and the gels were stained with ethidium bromide. The intensities of the shifted bands were quantified using a Gel Doc EZ imager and Image Lab software (Bio-Rad, Japan).

Results and discussion

Cryo-EM analysis of the hTUT1:U6 snRNA complex

To elucidate the interactions between hTUT1 and U6 snRNA, we conducted a cryo-EM analysis of full-length hTUT1 in complex with full-length U6 snRNA (Figure 1A and B). The hTUT1:U6 snRNA complex was reconstituted by mixing full-length hTUT1 (1–874 aa) with full-length U6 snRNA bearing four uridines at its 3′-end (106 nt). hTUT1 and U6 snRNA formed a stable complex, which was purified by size-exclusion chromatography for cryo-EM analysis.

Two datasets were collected. By merging the two datasets, we successfully obtained a consensus map at 3.2-Å resolution (Supplementary Figure S1). Focused 3D classification on the regions corresponding to the 5′-short stem-loop of U6 snRNA and the ISL of U6 snRNA and KA-1 domain of hTUT1 in the complex improved the quality of their cryo-EM maps (Supplementary Figure S1). Using the composite map combining these maps, the structural model of the hTUT1:U6 snRNA complex was built and refined (Figure 1C and D and Table 1, and Supplementary Figures S1 and S2).

In the final structural model, several regions of hTUT1 were not modeled due to poor cryo-EM map quality: the N-terminal residues (amino acid residues 1–5), the linker between RRM and Fingers (amino acid residues 132–144), the proline-rich region (PRR, amino acid residues 224–332), the region around the NLS (amino acid residues 639–762) and the C-terminal expression tag (hexa-histidine tag) were not modeled (Figure 1C and E, and Supplementary Figure S4). The statistics for the cryo-EM analysis and refinement are summarized in Table 1.

Overall structure of the hTUT1:U6 snRNA complex

The cryo-EM structure of the hTUT1:U6 snRNA complex reveals extensive interactions between the multi-domain hTUT1 and U6 snRNA (Figure 1D and E, and

Table 1. Cryo-EM data collection, refinement and validation statistics

	#1 High-resolution consensus map (EMDB 61234)	#2 KA-1-ISL focused map (EMDB 61235)	#3 5′-short stem-loop focused map (EMDB 61236)	#4 Composite map (PDB 9J8P) (EMDB 61237)
Data collection and processing				
Magnification	105 000	105 000	105 000	
Voltage (kV)	300	300	300	
Electron exposure (e–/Å^2)	50	50	50	
Defocus range (μm)	−0.8 to −1.8	−0.8 to −1.8	−0.8 to −1.8	
Pixel size (Å)	0.83	0.83	0.83	
Symmetry imposed	C1	C1	C1	
Initial particle images (no.)	17 065 245	17 065 245	17 065 245	
Final particle images (no.)	263 158	44 327	46 416	
Map resolution (Å)	3.21	3.83	3.72	
FSC threshold	0.143	0.143	0.143	
Refinement				
Initial model used (PDB code)				8IDF, 5WU1
Map-Model FSC (masked) (Å)				2.67
FSC threshold				0.5
Postprocessing				EMReady
Map correlation coefficients				
CC_mask				0.84
CC_volume				0.84
Model composition				
Non-hydrogen atoms				7062
Protein residues				623
RNA residues				106
Ligands (Zn)				1
B factors (Å^2)				
Protein				128.36
RNA				203.87
Ligand				109.97
R.m.s. deviations				
Bond lengths (Å)				0.003
Bond angles (°)				0.606
Validation				
MolProbity score				1.90
Clashscore				11.53
Poor rotamers (%)				0
Ramachandran plot				
Favored (%)				95.28
Allowed (%)				4.72
Disallowed (%)				0

Supplementary Movie S1). Some of these interactions were previously observed in the crystal structure of hTUT1_ΔC, which lacks the KA-1 domain, in complex with U6_mini, which lacks the 5′-short stem-loop and the ISL (hTUT1_ΔC:U6_mini) (Figure 2A). In the hTUT1:U6 snRNA complex structure, the entire U6 snRNA structure and the entire multi-domain hTUT1 structure were modeled. Specifically, the 5′-short stem-loop and the ISL of U6 snRNA were modeled, and the interactions between the ISL and the KA-1 domain of hTUT1 were observed and modeled (Figures 1D and E and 2B). The resolution for ISL-KA-1 and 5′-short stem-loop RNA is relatively low compared with that of the central region (Supplementary Figures S2 and S3). However, our potential map clearly depicts the characteristic features of the RNA stem-loop in both the 5′-stem and ISL (Figure 1F–I). The map shows good continuity and is free from anisotropy, allowing us to interpret and construct a reliable model. The potential map corresponding to KA-1 aligns well with the domain's secondary structure, with helices represented as tubular densities and the β-sheet as a sheet-like density. The linker between the Fingers and KA-1 domains is also clearly visible in the density map, further reinforcing the model. Furthermore, this model is consistent with previous Tb (III)-mediated cleavage assays conducted in the presence and absence of hTUT1 (and its variants), as described below. While the final model is mechanistically reasonable, alternative structural fits for these regions cannot be entirely ruled out.

Together, the N-terminal ZF, RRM and Palm capture and surround the single-stranded AUA motif between the 5′-short stem-loop and the telestem, relocating the 3′-end of the double-stranded telestem to the catalytic cleft between the Palm and Fingers (Figure 1E). The structure of the 5′-short stem-loop of U6 snRNA would ensure that the single-stranded region containing the AUA motif is held by the N-terminal ZF–RRM and the Palm, thus preventing its dissociation. Furthermore, the root region of the 5′-short stem-loop interacts with the RRM of hTUT1, as described below. Thus, the 5′-short stem-loop of U6 snRNA acts as an anchor that impedes the dissociation of U6 snRNA from hTUT1. The double-stranded telestem is gripped by the N-terminal ZF and Fingers, thereby positioning the 3′-end of the U6

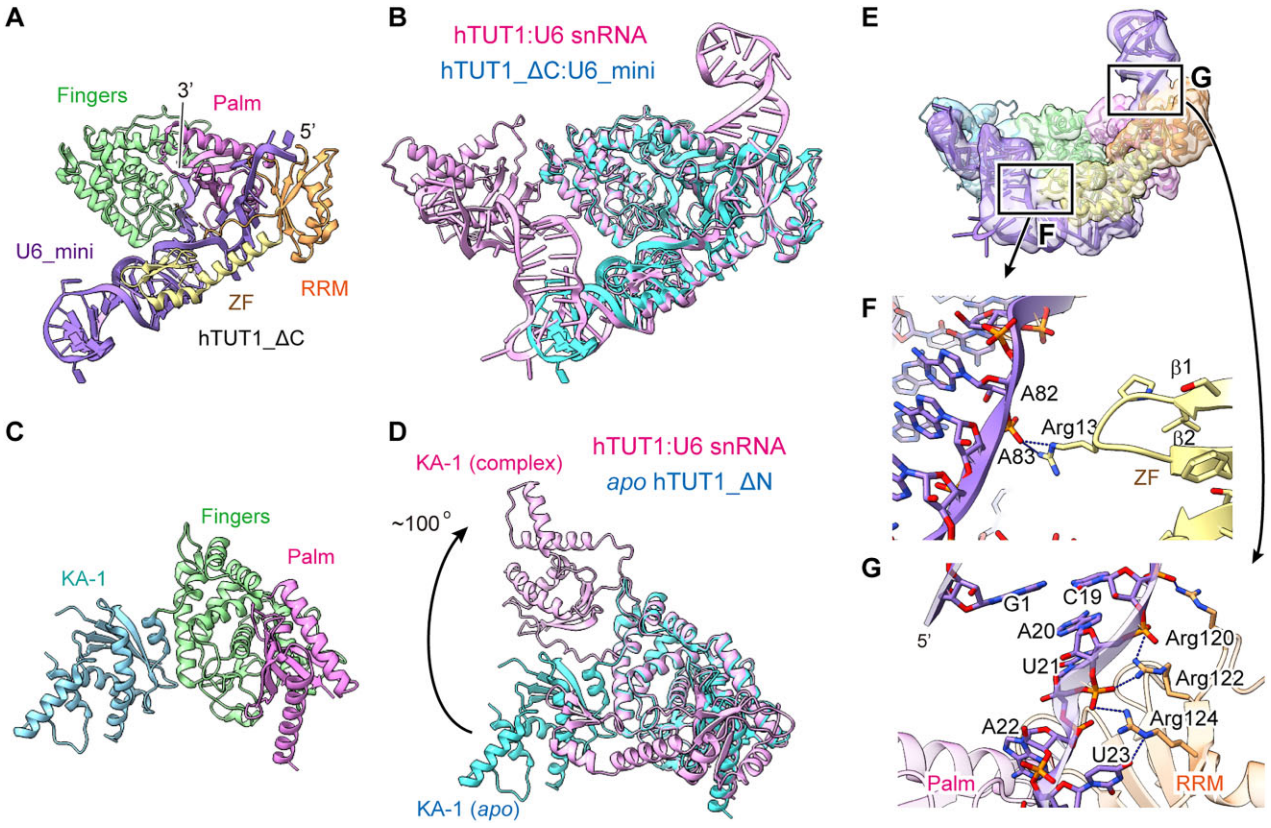

Figure 2. Structural comparisons between hTUT1:U6 snRNA complex and hTUT1 variants and their complexes with RNA. (**A**) Crystal structure of the hTUT1_ΔC:U6_mini complex (PDB ID: 8IDF) (23). ZF, RRM, Palm, Fingers and RNA are colored as in Figure 1E. (**B**) Superimposition of the cryo-EM structure of hTUT1:U6 snRNA (magenta) and the crystal structure of hTUT1_ΔC:U6_mini (cyan). (**C**) Crystal structure of *apo* hTUT1_ΔN, lacking the N-terminal ZF-RRM (PDB ID: 5WU1) (20). (**D**) Superimposition of the hTUT1:U6 snRNA (magenta) and *apo* hTUT1_ΔN (cyan). (**E**) Cartoon representation of the hTUT1:U6 snRNA complex overlayed with the cryo-EM composite map. The regions enlarged in panels (F) and (G) are indicated. (**F**) Detailed views of the interactions between U6 snRNA and ZF. (**G**) Detailed views of the interaction between U6 snRNA and RRM. ZF, RRM, Palm, Fingers, KA-1 and RNA in panels (A), (C) and (E–G) are colored as in Figure 1.

snRNA at the catalytic site for oligo-uridylylation. The 3′-terminal U106 of the U6 snRNA resides in the UTP binding site; thus, the structure represents the post-U106 addition stage (Supplementary Figure S3C). In the hTUT1:U6 snRNA complex structure, the C-terminal KA-1 domain holds the tip of the ISL of U6 snRNA (Figure 1E), as described below in detail, causing the 3′-stem region of U6 snRNA to adopt a bent conformation between the ISL and the telestem (Figures 1B and E and 2B).

The previous crystal structure of *apo* hTUT1 lacking the N-terminal ZF domain and RRM (hTUT1_ΔN) (Figure 2C, and Supplementary Figure S5) showed that the C-terminal KA-1 domain is mobile relative to the catalytic Palm and Fingers (20). Superimposition of the hTUT1:U6 snRNA complex and *apo* hTUT1_ΔN structures revealed the rotation of the KA-1 domain by ∼100 degrees relative to the catalytic Palm and Fingers upon U6 snRNA binding to hTUT1 (Figure 2D, and Supplementary Figure S5). In the hTUT1:U6 snRNA complex structure, the 3′-stem of U6 snRNA adopts a bent conformation between the telestem and ISL, and the ZF interacts with the bent region (Figure 2E). Arg13, between β1 and β2 in the ZF, forms hydrogen bonds with the phosphate backbone of A83 (Figures 1B and 2F). In the crystal structure of hTUT1_ΔC:U6_mini, the N-terminal RRM interacts with the A22U23A24 motif located in the 5′-part of U6_mini in a base-specific manner (23). In the hTUT1:U6 snRNA complex structure, additional interactions between the RRM and the upstream C19A20U21, in the single-stranded region between the 5′-short stem-loop and the telestem, were also observed (Figure 2E). Arg120, Arg122 and Arg124 form hydrogen bonds with the phosphate backbones of C19, A20 and U21, respectively (Figures 1B and 2G). Arg13, Arg120, Arg122 and Arg124 are highly conserved among TUT1 enzymes, indicating the importance of the interactions between the AUA motif of U6 snRNA and the RRM of TUT1 (Supplementary Figure S4).

Altogether, the multi-domain hTUT1 holds the entire body of U6 snRNA and recognizes its specific sequence and structural features for efficient oligo-uridylylation.

Recognition of ISL of U6 snRNA by KA-1 domain of hTUT1

Previous biochemical studies demonstrated that the C-terminal KA-1 domain of hTUT1 acts as an RNA-binding domain (20). While it was suggested that the arginine-rich region (RRR) in KA-1 interacts with the 3′-stem of U6 snRNA, the detailed interactions between KA-1 and U6 snRNA remained unclear. The hTUT1:U6 snRNA complex structure revealed that KA-1 interacts with the ISL of U6 snRNA (Figure 1D and E). The tip of the ISL interacts with the positively charged surface of the KA-1 domain, and the phosphate backbone

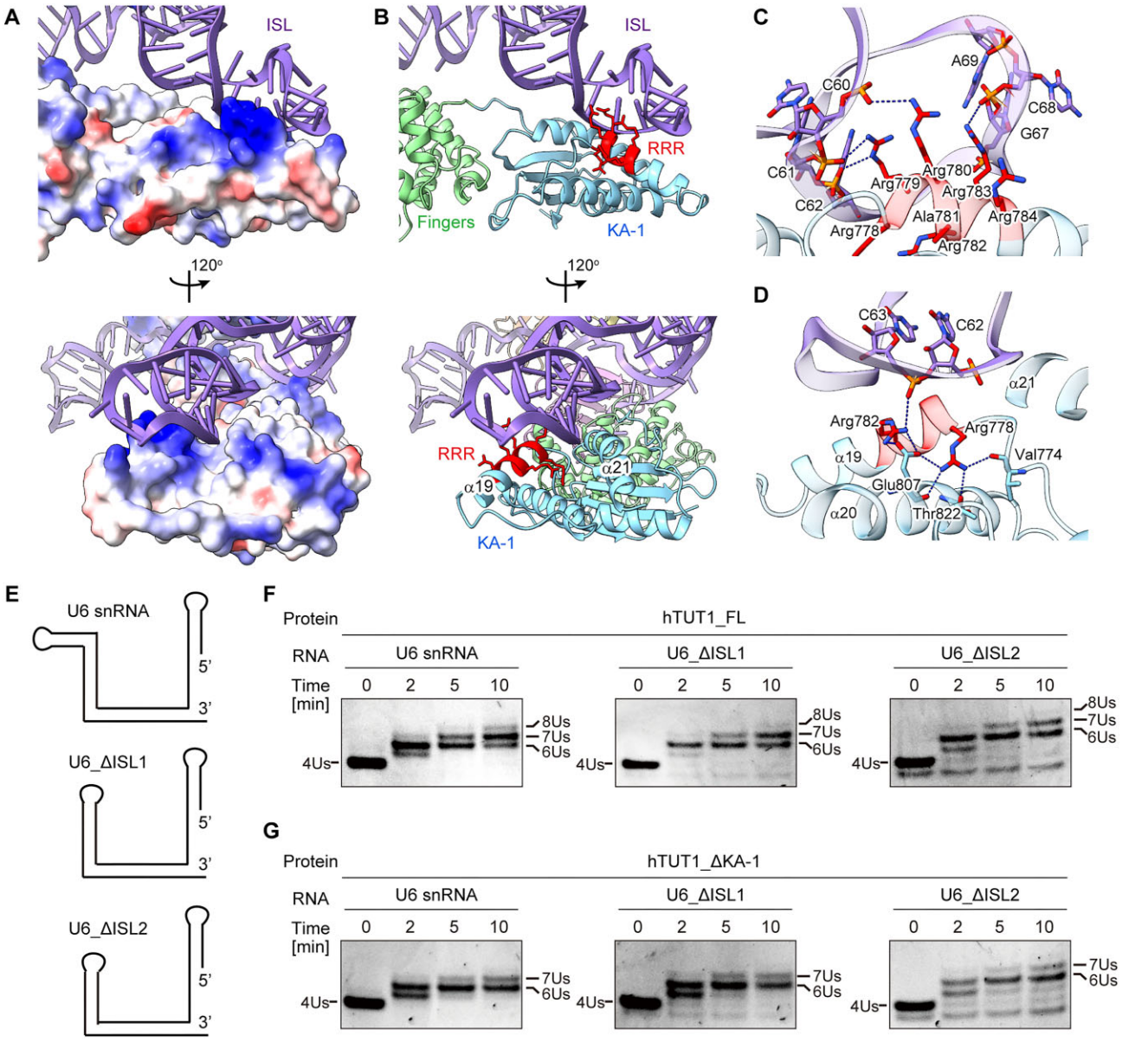

Figure 3. Interactions between KA-1 and ISL of U6 snRNA. (**A**) The interactions between KA-1 of hTUT1 and the ISL of U6 snRNA. U6 snRNA is shown in a cartoon representation. hTUT1 is shown in an electrostatic surface representation. Positively and negatively charged areas are colored blue and red, respectively. (**B**) Cartoon representation of panel (A). Fingers and KA-1 are colored green and cyan, respectively, and the RRR in KA-1 is colored red. (**C** and **D**) Detailed views of the interactions between KA-1 and ISL. (**E**) Schematic presentation of U6 snRNA and its variants (U6_ΔISL1 and U6_ΔISL2) used for the uridylylation assays. The detailed secondary structure is shown in Supplementary Figure S6. (**F**) Uridylylation of U6 snRNA and its variants in panel (E) by full-length hTUT1. (**G**) Uridylylation of U6 snRNA and its variants in panel (E) by hTUT1_ΔC lacking KA-1. RNA (25 nM; U6 snRNA or its variants) was incubated with 20 nM hTUT1 or hTUT1_ΔC in the presence of 1 mM UTP at 37°C.

aligns within the shallow groove between helices α19 and α21 (Figure 3A and B). The conserved RRR motif (R778-R779-R780-A781-R782-R783-R784) (Supplementary Figure S4) in the α19 helix engages with the major groove of the ISL (Figure 3B). Specifically, Arg779 forms hydrogen bonds with the phosphate groups of C61 and C62, while Arg780, Arg782 and Arg783 form hydrogen bonds with the phosphate groups of C60, C63 and C68, respectively (Figure 3C). Base-specific interactions were not observed between the ISL and the RRR in KA-1. Thus, the KA-1 domain recognizes the structure of the tip of the ISL, rather than the sequence. Consistent with the structure, the R779A/R783A double mutation abolished the RNA-binding capability of the KA-1 domain, and displayed reduced uridylylation activity *in vitro* (20). Furthermore, Arg778 and Arg782 contribute to the stabilization of the domain structure through intramolecular hydrogen bonds (Figure 3D). Arg778 and Arg782 in α19 form hydrogen bonds with Glu807 in α20, and Arg778 also forms hydrogen bonds with the main chain carbonyl oxygens of Val774 and Thr822 (Figure 3D).

To explore the role of the ISL of U6 snRNA in U6 snRNA recognition and oligo-uridylylation by hTUT1, mutant U6 snRNAs with shorter ISLs (U6_ΔISL1 and U6_ΔISL2) and 3′- 4Us (Figure 3E, and Supplementary Figure S6) were tested for oligo-uridylylation by full-length hTUT1 or hTUT1 lacking KA-1 (hTUT1_ΔC) *in vitro* (Figure 3F and G). The mutant

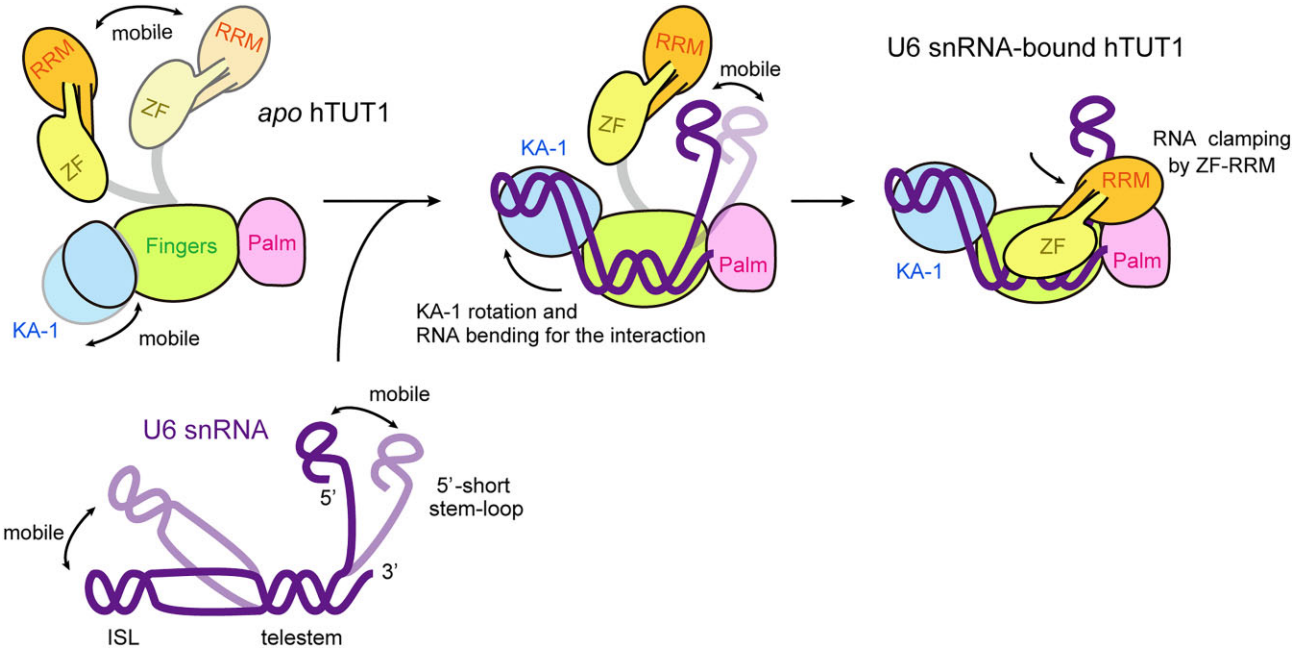

Figure 4. Domain movements for U6 snRNA oligo-uridylylation by hTUT1. Schematic diagram of U6 snRNA recognition by multiple domains of hTUT1. ZF, RRM, Palm, Fingers and KA-1 domains of hTUT1 are colored orange, magenta, green and cyan, respectively. U6 snRNA is represented by purple lines. The N-terminal ZF-RRM and the C-terminal KA-1 domain are mobile relative to the catalytic Palm-Fingers. The 5′-short stem-loop and 3′-stem, consisting of telestem and ISL, are flanked by a single-stranded AUA motif. The 5′-short stem-loop is mobile relative to the telestem, and the 3′-stem could adopt either an extended or a bent conformation.

U6 snRNAs were designed based on the predicted secondary and tertiary structures of U6 snRNA. In U6_ΔISL1 and U6_ΔISL2, the 5′-short stem-loop and telestem are expected to maintain secondary structures similar to those in full-length U6 snRNA, as predicted by AlphaFold3 (Supplementary Figure S6). Furthermore, full-length hTUT1 bound to all three RNAs with comparable affinities, suggesting that the mutant RNAs (U6_ΔISL1 and U6_ΔISL2) adopt conformations similar to full-length U6 snRNA, as predicted. The hTUT1_ΔC mutant also bound all three RNAs with comparable affinities, albeit slightly weaker than full-length hTUT1 (Supplementary Figure S7). These results support the similar secondary structures shared by these three RNAs.

Full-length hTUT1 oligo-uridylylated U6_ΔISL1 and U6_ΔISL2 less efficiently than full-length U6 snRNA (Figure 3F). hTUT1 extended the oligo-uridine tail of U6 snRNA to 3′-7Us more rapidly than U6_ΔISL1 and U6_ΔISL2, and extends to 3′-8Us. Furthermore, hTUT1_ΔC uridylylated U6_ΔISL1 and U6_ΔISL2 to the same extent as full-length U6 snRNA and extends the oligo-uridine tail of U6 snRNA and its variants to 3′-7Us, while hTUT1_ΔC uridylated full-length U6 snRNA less efficiently than full-length hTUT1 (Figure 3G). These results suggest the recognition of the ISL by the KA-1 domain. A previous biochemical study demonstrated that hTUT1 mutants, hTUT1_ΔC or R779A/R783A, add fewer UMPs to U6 snRNA, as compared with full-length hTUT1 (20). The absence of KA-1 or the loss of its RNA binding activity would allow the U6 snRNA to shift or dislodge easily on the enzyme surface due to its lowered affinity for the U6 snRNA. Consequently, the U6 snRNA would be released from the enzyme, leading to fewer UMP incorporations on the 3′-end of U6 snRNA.

Altogether, the KA-1 domain recognizes the structure of the ISL of U6 snRNA, and its interactions with the ISL anchor the U6 snRNA on the hTUT1 surface for efficient oligo-uridylylation.

Domain arrangement of hTUT1 and U6 snRNA conformation change

In *apo* hTUT1, both the N-terminal ZF–RRM and C-terminal KA-1 domain are mobile relative to the Palm and Fingers (Figure 2D, and Supplementary Figure S5B–D) (20,23). The multiple domains of hTUT1 hold the entire U6 snRNA body and position the 3′-end of U6 snRNA in the catalytic pocket, using the mobile N-terminal ZF–RRM and C-terminal KA-1 domain (Figures 1 and 4). Upon telestem binding to the catalytic Palm and Fingers of hTUT1, the interactions of the mobile N-terminal ZF–RRM and the C-terminal KA-1 domain with specific positions in the U6 snRNA ensure the proper placement of the 3′-end of U6 snRNA in the active catalytic site, and the efficient oligo-uridylylation of the RNA proceeds.

Previous biochemical studies on the interactions between hTUT1 (or its variants) and U6 snRNA by Tb (III)-mediated RNA foot-printing (34) allowed us to predict the hTUT1 binding sites on the U6 snRNA and its structural changes (Supplementary Figure S8) (20). The RNA foot-printing revealed that several nucleotides (A48–A53, A83–A92 and C68) were deprotected in a KA-1-dependent manner (Supplementary Figure S8A) (20). In the hTUT1:U6 snRNA complex, nucleotides A48–A53 and A83–A92 are located at the bent corner between the telestem and the ISL of U6 snRNA, while C68 is in the pentaloop of the ISL (Supplementary Figure S8B). Considering the biochemical study of Tb (III)-mediated U6 snRNA foot-printing and the present structure, the positioning of the C-terminal KA-1 domain at the ISL of the U6 snRNA would induce a conformational change of the 3′-stem region structure, which could intrinsically adopt alternative extended and bent con-

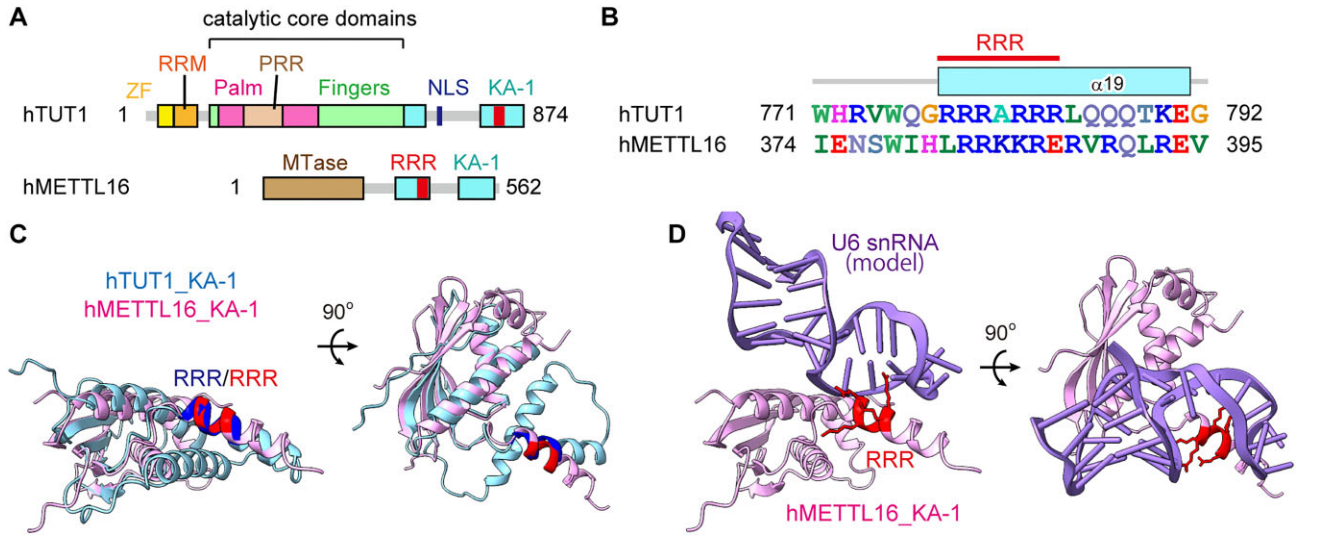

Figure 5. Comparison of the KA-1 domains of hTUT1 and hMETTL16. (**A**) Schematic diagrams of full-length hTUT1 and human METTL16 (hMETTL16). ZF, RRM, Palm, Fingers and KA-1 of hTUT1 are colored yellow, orange, magenta, green and cyan, respectively. The MTase and KA-1 domains of hMETTL16 are colored brown and cyan, respectively. The RRRs in hTUT1 and hMETTL16 are colored red. (**B**) Sequence alignment around the KA-1 RRRs of hTUT1 and hMETTL16. The secondary structure of hTUT1 is shown. (**C**) Superimposition of the KA-1 domain of hTUT1 (35) (cyan, PDB ID: 6M1U) and the AlphaFold2-modeled KA-1 of hMETTL16 (magenta). The RRRs of hTUT1 and hMETTL16 are colored blue and red, respectively. (**D**) Docking model of the ISL of U6 snRNA onto the KA-1 of hMETTL16. The KA-1 domain and U6 snRNA are colored magenta and purple, respectively, and the RRR is shown in red.

formations, and fix the 3′-stem region in a bent conformation (Figure 4). Structural modulations of the ISL loop would also be induced by the interactions with the RRR in KA-1.

The arrangement/movement of hTUT1 domains for U6 snRNA recognition and oligo-uridylylation also aptly explains the results of previous biochemical kinetic studies (20). For instance, the deletion of the N-terminal ZF–RRM (hTUT1_ΔN) decreased the k_{cat} value for oligo-uridylylation more severely than the deletion of the C-terminal KA-1domain (hTUT1_ΔC) (0.13 s^{-1} for hTUT1_ΔC and 0.0003 s^{-1} for hTUT1_ΔN) (20). Conversely, while both hTUT1_ΔN and hTUT1_ΔC have reduced affinities for U6 snRNA, the affinity of hTUT1_ΔC for U6 snRNA is weaker than hTUT1_ΔN: the K_m values of hTUT1_ΔC and hTUT1_ΔN for U6 snRNA were 558 and 377 nM, respectively (20). Thus, upon hTUT1 binding to U6 snRNA, using the catalytic core region, the mobile KA-1 interacts with tip of the ISL, leading the 3′-stem of U6 snRNA to adopt the bent conformation. The interaction between the KA-1 domain and the ISL of U6 snRNA, as well as the conformation transition of U6 snRNA to the bent-form, would increase the affinity of the U6 snRNA for hTUT1 during the elongation stage of U6 snRNA oligo-uridylylation, thereby decreasing K_m. The mobile N-terminal ZF and RRM hook the single-stranded region between the 5′-short stem-loop, positioning the 3′-end of the U6 snRNA in the catalytic pocket for efficient oligo-uridylylation (Figure 4). This domain movement ensures the catalysis of oligo-uridylylation, thereby enhancing k_{cat}. The hTUT1:U6 snRNA complex would be further stabilized through the interactions of the loop between β1 and β2 in the ZF and the phosphate backbone of the bent corner between the telestem and the ISL, which would also increase the affinity of U6 snRNA for hTUT1 and facilitate the catalysis (Figure 2E and F).

KA-1 domain homolog in METTL16

A structure homologous to KA-1, containing the RRR, has been identified in the C-terminal region of eukaryotic METTL16, an N^6-methyladenosine (m^6A) methyltransferase (MTase) (35,36) (Figure 5A and B). Eukaryotic METTL16 and its homologs comprise two domains: the N-terminal methyltransferase domain and the C-terminal domain (37–39). The C-terminal domain was originally termed the vertebrate-conserved region, but later renamed a KA-1, and is conserved among eukaryotes (35,36).

Human METTL16 (hMETTL16) methylates adenosine at position 43 (A43) of U6 snRNA for 5′-splice site recognition of specific pre-mRNAs (40–43). METTL16 also methylates specific adenosines in the 3′ untranslated region of the SAM (S-adenosylmethionine) synthetase (MAT2A) mRNA, regulates MAT2A mRNA splicing and controls the SAM concentration homeostasis in cells (42–45).

A previous biochemical study suggested that the KA-1 of hMETTL16 interacts with the ISL of U6 snRNA, increasing the affinity of hMETTL16 for U6 snRNA (35). Furthermore, the KA-1 of hMETTL16 could be replaced with that of hTUT1 for the methylation of A43 of U6 snRNA *in vitro* (35), suggesting that the KA-1 domains of hMETTL16 and hTUT1 perform similar functions in the specific recognition of the U6 snRNA. While the crystal structure of the C-terminal KA-1 domain of hMETTL16 was reported, the RRR in the KA-1 domain was not modeled due to its poor electron density (35). Thus, we compared the structure of the KA-1 domain of hTUT1 and an AlphaFold predicted model of KA-1 of hMETTL16 (UniProt ID: Q86W50) (46,47). The domain structures, including the RRRs, of hTUT1 and hMETTL16 are well-aligned (Figure 5C, and Supplementary Figure S9). A docking model of U6 snRNA onto KA-1 of hMETTL16 shows that the tip of the ISL of U6 snRNA could bind to the KA-1 of hMETTL16 in a similar manner to the KA-1 of hTUT1 (Fig-

ure 5D). The recognition of the ISL of U6 snRNA by the KA-1 domain might be conserved between hTUT1 and hMETTL16. The detailed mechanism of U6 snRNA recognition by the KA-1 domain of hMETTL16 awaits further structural analysis.

Conclusion

In this study, we have presented the cryo-EM structure of full-length hTUT1 in complex with full-length U6 snRNA (Figure 1). The structure advances our understanding of how the multi-domain hTUT1 recognizes the structured U6 RNA, which was not fully clarified in the previous crystal structure of a truncated hTUT1 (hTUT1_ΔC) in complex with a shortened U6 snRNA (U6_mini) (23). Specifically, the present hTUT1:U6 snRNA complex structure captured the 5′-short stem-loop of U6 snRNA anchoring the U6 snRNA itself to hTUT1 and facilitating the relocation of the telestem within the catalytic cleft of hTUT1 (Figures 1E and 4). The structure also revealed the C-terminal KA-1 domain interacting with the ISL of the U6 snRNA via an RRR, anchoring the U6 snRNA to hTUT1 (Figures 1E and 3A–C). KA-1 binding to the tip of the ISL induces the conformational transition of the 3′-stem of U6 snRNA to the bent conformation between the telestem and the ISL, and the N-terminal ZF-RRM and the Palm clamp the AUA motif between the 5′-short stem-loop and the telestem, positioning the 3′-end of U6 snRNA in the catalytic site for oligo-uridylylation (Figure 4). hTUT1 recognizes specific sequence and structural features of the U6 snRNA and holds the entire body of the U6 snRNA. Thus, hTUT1 is a U6 snRNA-specific TUTase, distinguishing it from other TUTases, TUT4/TUT7, that act on different RNA substrates (12,13,19,48,49). Dysfunctions in enzymes involved in U6 snRNA maturation are associated with various diseases and developmental disorders. Mpn1 (USB1), a nuclease essential for trimming the 3′ oligo-uridylylated tail synthesized by hTUT1 for U6 snRNA maturation, is associated with poikiloderma with neutropenia (7,14–16,50). METTL16, an m^6A methylase that modifies A43 of U6 snRNA (42,43,45), regulates specific pre-mRNA splicing and is essential for embryonic development (38). While the involvement of TUT1 dysfunctions in diseases remains unclear, the critical role of U6 snRNA maturation in splicing suggests that hTUT1 dysfunctions may lead to altered mRNA metabolism. The structural details presented here offer insights into the molecular mechanisms of hTUT1-related diseases and potential targeted therapies.

Data availability

The atomic coordinates of the TUT1:U6 snRNA complex have been deposited in the Protein Data Bank (PDB 9J8P). The composite and high-resolution consensus EM maps for the TUT1:U6 snRNA complex have been deposited in the Electron Microscopy Data bank (EMD-61237 and EMD-61234, respectively). The KA1_ISL and the 5′-short stem-loop focused EM maps for the TUT1:U6 snRNA complex have been deposited in the Electron Microscopy Data bank (EMD-61235 and EMD-61236, respectively). The micrographs of TUT1:U6 snRNA have been deposited in the Electron Microscopy Public Image Archive (EMPIAR-12277).

Supplementary data

Supplementary Data are available at NAR Online.

Acknowledgements

We thank staff of the Cryo-Electron Microscopy Facility at the University of Tokyo for technical assistance during data collection.

Funding

JSPS [LS135, 23H00368, 18H03980 and 26251009 to K.T.; 19K16053 to S.Y.]; Ministry of Education, Culture, Sports, Science and Technology [26113002 to K.T.]; Uehara Memorial Foundation [to K.T.]; Terumo Foundation for Life Sciences and Arts [to K.T.]; Princess Takamatsu Cancer Research Fund [to K.T.]; AMED [JP23ama121002]. Funding for open access charge: JSPS.

Conflict of interest statement

None declared.

References

1. Will,C.L. and Luhrmann,R. (2011) Spliceosome structure and function. *Cold Spring Harb. Perspect. Biol.*, **3**, a003707.
2. Jandrositz,A. and Guthrie,C. (1995) Evidence for a Prp24 binding site in U6 snRNA and in a putative intermediate in the annealing of U6 and U4 snRNAs. *EMBO J.*, **14**, 820–832.
3. Raghunathan,P.L. and Guthrie,C. (1998) A spliceosomal recycling factor that reanneals U4 and U6 small nuclear ribonucleoprotein particles. *Science*, **279**, 857–860.
4. Achsel,T., Brahms,H., Kastner,B., Bachi,A., Wilm,M. and Luhrmann,R. (1999) A doughnut-shaped heteromer of human Sm-like proteins binds to the 3′-end of U6 snRNA, thereby facilitating U4/U6 duplex formation *in vitro*. *EMBO J.*, **18**, 5789–5802.
5. Fica,S.M., Tuttle,N., Novak,T., Li,N.S., Lu,J., Koodathingal,P., Dai,Q., Staley,J.P. and Piccirilli,J.A. (2013) RNA catalyses nuclear pre-mRNA splicing. *Nature*, **503**, 229–234.
6. Didychuk,A.L., Butcher,S.E. and Brow,D.A. (2018) The life of U6 small nuclear RNA, from cradle to grave. *RNA*, **24**, 437–460.
7. Mroczek,S. and Dziembowski,A. (2013) U6 RNA biogenesis and disease association. *Wiley Interdiscip. Rev. RNA*, **4**, 581–592.
8. Trippe,R., Sandrock,B. and Benecke,B.J. (1998) A highly specific terminal uridylyl transferase modifies the 3′-end of U6 small nuclear RNA. *Nucleic Acids Res.*, **26**, 3119–3126.
9. Trippe,R., Richly,H. and Benecke,B.J. (2003) Biochemical characterization of a U6 small nuclear RNA-specific terminal uridylyltransferase. *Eur. J. Biochem.*, **270**, 971–980.
10. Trippe,R., Guschina,E., Hossbach,M., Urlaub,H., Luhrmann,R. and Benecke,B.J. (2006) Identification, cloning, and functional analysis of the human U6 snRNA-specific terminal uridylyl transferase. *RNA*, **12**, 1494–1504.
11. Lee,M., Kim,B. and Kim,V.N. (2014) Emerging roles of RNA modification: m(6)A and U-tail. *Cell*, **158**, 980–987.
12. Yu,S. and Kim,V.N. (2020) A tale of non-canonical tails: gene regulation by post-transcriptional RNA tailing. *Nat. Rev. Mol. Cell Biol.*, **21**, 542–556.
13. Liudkovska,V. and Dziembowski,A. (2021) Functions and mechanisms of RNA tailing by metazoan terminal nucleotidyltransferases. *Wiley Interdiscip. Rev. RNA*, **12**, e1622.
14. Hilcenko,C., Simpson,P.J., Finch,A.J., Bowler,F.R., Churcher,M.J., Jin,L., Packman,L.C., Shlien,A., Campbell,P., Kirwan,M., *et al.* (2013) Aberrant 3′ oligoadenylation of spliceosomal U6 small nuclear RNA in poikiloderma with neutropenia. *Blood*, **121**, 1028–1038.
15. Mroczek,S., Krwawicz,J., Kutner,J., Lazniewski,M., Kucinski,I., Ginalski,K. and Dziembowski,A. (2012) C16orf57, a gene mutated in poikiloderma with neutropenia, encodes a putative

phosphodiesterase responsible for the U6 snRNA 3′ end modification. *Genes Dev.*, **26**, 1911–1925.
16. Shchepachev,V., Wischnewski,H., Missiaglia,E., Soneson,C. and Azzalin,C.M. (2012) Mpn1, mutated in poikiloderma with neutropenia protein 1, is a conserved 3′-to-5′ RNA exonuclease processing U6 small nuclear RNA. *Cell Rep.*, **2**, 855–865.
17. Achsel,T., Brahms,H., Kastner,B., Bachi,A., Wilm,M. and Lührmann,R. (1999) A doughnut-shaped heteromer of human Sm-like proteins binds to the 3′-end of U6 snRNA, thereby facilitating U4/U6 duplex formation *in vitro*. *EMBO J.*, **18**, 5789–5802.
18. Vidal,V.P., Verdone,L., Mayes,A.E. and Beggs,J.D. (1999) Characterization of U6 snRNA–protein interactions. *RNA*, **5**, 1470–1481.
19. Yashiro,Y. and Tomita,K. (2018) Function and regulation of human terminal uridylyltransferases. *Front. Genet.*, **9**, 538.
20. Yamashita,S., Takagi,Y., Nagaike,T. and Tomita,K. (2017) Crystal structures of U6 snRNA-specific terminal uridylyltransferase. *Nat. Commun.*, **8**, 15788.
21. Rinke,J. and Steitz,J.A. (1985) Association of the lupus antigen La with a subset of U6 snRNA molecules. *Nucleic Acids Res.*, **13**, 2617–2629.
22. Karaduman,R., Fabrizio,P., Hartmuth,K., Urlaub,H. and Lührmann,R. (2006) RNA structure and RNA–protein interactions in purified yeast U6 snRNPs. *J. Mol. Biol.*, **356**, 1248–1262.
23. Yamashita,S. and Tomita,K. (2023) Mechanism of U6 snRNA oligouridylation by human TUT1. *Nat. Commun.*, **14**, 4686.
24. Kao,C., Zheng,M. and Rüdisser,S. (1999) A simple and efficient method to reduce nontemplated nucleotide addition at the 3 terminus of RNAs transcribed by T7 RNA polymerase. *RNA*, **5**, 1268–1272.
25. Schürer,H., Lang,K., Schuster,J. and Mörl,M. (2002) A universal method to produce *in vitro* transcripts with homogeneous 3′ ends. *Nucleic Acids Res.*, **30**, e56.
26. Punjani,A., Rubinstein,J.L., Fleet,D.J. and Brubaker,M.A. (2017) cryoSPARC: algorithms for rapid unsupervised cryo-EM structure determination. *Nat. Methods*, **14**, 290–296.
27. Rubinstein,J.L. and Brubaker,M.A. (2015) Alignment of cryo-EM movies of individual particles by optimization of image translations. *J. Struct. Biol.*, **192**, 188–195.
28. He,J., Li,T. and Huang,S.-Y. (2023) Improvement of cryo-EM maps by simultaneous local and non-local deep learning. *Nat. Commun.*, **14**, 3217.
29. Sarzynska,J., Popenda,M., Antczak,M. and Szachniuk,M. (2023) RNA tertiary structure prediction using RNAComposer in CASP15. *Proteins*, **91**, 1790–1799.
30. Emsley,P., Lohkamp,B., Scott,W.G. and Cowtan,K. (2010) Features and development of Coot. *Acta Crystallogr. D Biol. Crystallogr.*, **66**, 486–501.
31. Afonine,P.V., Grosse-Kunstleve,R.W., Echols,N., Headd,J.J., Moriarty,N.W., Mustyakimov,M., Terwilliger,T.C., Urzhumtsev,A., Zwart,P.H. and Adams,P.D. (2012) Towards automated crystallographic structure refinement with phenix.Refine. *Acta Crystallogr. D Biol. Crystallogr.*, **68**, 352–367.
32. Liebschner,D., Afonine,P.V., Baker,M.L., Bunkóczi,G., Chen,V.B., Croll,T.I., Hintze,B., Hung,L.W., Jain,S., McCoy,A.J., *et al.* (2019) Macromolecular structure determination using X-rays, neutrons and electrons: recent developments in Phenix. *Acta Crystallogr. D Struct. Biol.*, **75**, 861–877.
33. Meng,E.C., Goddard,T.D., Pettersen,E.F., Couch,G.S., Pearson,Z.J., Morris,J.H. and Ferrin,T.E. (2023) UCSF ChimeraX: tools for structure building and analysis. *Protein Sci.*, **32**, e4792.
34. Walter,N.G., Yang,N. and Burke,J.M. (2000) Probing non-selective cation binding in the hairpin ribozyme with Tb(III). *J. Mol. Biol.*, **298**, 539–555.
35. Aoyama,T., Yamashita,S. and Tomita,K. (2020) Mechanistic insights into m6A modification of U6 snRNA by human METTL16. *Nucleic Acids Res.*, **48**, 5157–5168.
36. Ju,J., Aoyama,T., Yashiro,Y., Yamashita,S., Kuroyanagi,H. and Tomita,K. (2023) Structure of the *Caenorhabditis elegans* m6A methyltransferase METT10 that regulates SAM homeostasis. *Nucleic Acids Res.*, **51**, 2434–2446.
37. Ruszkowska,A., Ruszkowski,M., Dauter,Z. and Brown,J.A. (2018) Structural insights into the RNA methyltransferase domain of METTL16. *Sci. Rep.*, **8**, 5311.
38. Mendel,M., Chen,K.M., Homolka,D., Gos,P., Pandey,R.R., McCarthy,A.A. and Pillai,R.S. (2018) Methylation of structured RNA by the m(6)A writer METTL16 is essential for mouse embryonic development. *Mol. Cell*, **71**, 986–1000.
39. Doxtader,K.A., Wang,P., Scarborough,A.M., Seo,D., Conrad,N.K. and Nam,Y. (2018) Structural basis for regulation of METTL16, an S-adenosylmethionine homeostasis factor. *Mol. Cell*, **71**, 1001–1011.
40. Ishigami,Y., Ohira,T., Isokawa,Y., Suzuki,Y. and Suzuki,T. (2021) A single m(6)A modification in U6 snRNA diversifies exon sequence at the 5′ splice site. *Nat. Commun.*, **12**, 3244.
41. Shen,A., Hencel,K., Parker,M.T., Scott,R., Skukan,R., Adesina,A.S., Metheringham,C.L., Miska,E.A., Nam,Y., Haerty,W., *et al.* (2024) U6 snRNA m6A modification is required for accurate and efficient splicing of *C. elegans* and human pre-mRNAs. *Nucleic Acids Res.*, **52**, 9139–9160.
42. Pendleton,K.E., Chen,B., Liu,K., Hunter,O.V., Xie,Y., Tu,B.P. and Conrad,N.K. (2017) The U6 snRNA m(6)A methyltransferase METTL16 regulates SAM synthetase intron retention. *Cell*, **169**, 824–835.
43. Warda,A.S., Kretschmer,J., Hackert,P., Lenz,C., Urlaub,H., Höbartner,C., Sloan,K.E. and Bohnsack,M.T. (2017) Human METTL16 is a N6-methyladenosine (m^6A) methyltransferase that targets pre-mRNAs and various non-coding RNAs. *EMBO Rep.*, **18**, 2004–2014.
44. Watabe,E., Togo-Ohno,M., Ishigami,Y., Wani,S., Hirota,K., Kimura-Asami,M., Hasan,S., Takei,S., Fukamizu,A., Suzuki,Y., *et al.* (2021) m(6) A-mediated alternative splicing coupled with nonsense-mediated mRNA decay regulates SAM synthetase homeostasis. *EMBO J.*, **40**, e106434.
45. Shima,H., Matsumoto,M., Ishigami,Y., Ebina,M., Muto,A., Sato,Y., Kumagai,S., Ochiai,K., Suzuki,T. and Igarashi,K. (2017) S-adenosylmethionine synthesis is regulated by selective N(6)-adenosine methylation and mRNA degradation involving METTL16 and YTHDC1. *Cell Rep.*, **21**, 3354–3363.
46. Jumper,J., Evans,R., Pritzel,A., Green,T., Figurnov,M., Ronneberger,O., Tunyasuvunakool,K., Bates,R., Žídek,A., Potapenko,A., *et al.* (2021) Highly accurate protein structure prediction with AlphaFold. *Nature*, **596**, 583–589.
47. Varadi,M., Bertoni,D., Magana,P., Paramval,U., Pidruchna,I., Radhakrishnan,M., Tsenkov,M., Nair,S., Mirdita,M., Yeo,J., *et al.* (2023) AlphaFold Protein Structure Database in 2024: providing structure coverage for over 214 million protein sequences. *Nucleic Acids Res.*, **52**, D368–D375.
48. Faehnle,C.R., Walleshauser,J. and Joshua-Tor,L. (2017) Multi-domain utilization by TUT4 and TUT7 in control of let-7 biogenesis. *Nat. Struct. Mol. Biol.*, **24**, 658–665.
49. Yi,G., Ye,M., Carrique,L., El-Sagheer,A., Brown,T., Norbury,C.J., Zhang,P. and Gilbert,R.J.C. (2024) Structural basis for activity switching in polymerases determining the fate of let-7 pre-miRNAs. *Nat. Struct. Mol. Biol.*, **31**, 1426–1438.
50. Shchepachev,V. and Azzalin,C.M. (2013) The Mpn1 RNA exonuclease: cellular functions and implication in disease. *FEBS Lett.*, **587**, 1858–1862.

Received: September 5, 2024. **Revised:** December 14, 2024. **Editorial Decision:** December 20, 2024. **Accepted:** December 26, 2024